



Pseudo metallic (1T) molybdenum disulfide for efficient photo/electrocatalytic water splitting

Xitao Li^{a,b,c,1}, Xiangnan Sun^{c,1}, Haifeng Yu^c, Haotong Li^c, Xueyi Sun^b, Xia Tao^{c,*}, Yanzhen Zheng^{a,b,**}

^a State Key Laboratory of Advanced Metallurgy, University of Science and Technology Beijing, Beijing 100083, PR China

^b Beijing Key Laboratory of Green Recovery and Extraction of Rare and Precious Metals, University of Science and Technology Beijing, Beijing 100083, PR China

^c State Key Laboratory of Organic-Inorganic Composites, Beijing University of Chemical Technology, Beijing 100029, PR China

ARTICLE INFO

Keywords:

Pseudo-1 T MoS₂
Reducible species
Structure modulation
Low crystallinity
Photo/electrocatalytic water splitting

ABSTRACT

2D-layered metallic molybdenum disulfide i.e. 1T MoS₂ possess prominent electronic conductivity and abundant electrochemically active sites. However, tuning its metastable crystal structure for promoting catalytic performance is a big technical challenge. Here, we reveal the role of the intercalated reducible -NH and -NH₂ species as structural stabilizers in supporting the lamellar structure of 1T MoS₂, and then propose a novel H₂O₂-cleaning strategy to reduce the amount of reducible -NH and -NH₂ species for modulating the crystallinity and layer thickness of 1T MoS₂ without degrading to 2H MoS₂. The resultant pseudo-1T MoS₂ exhibits larger specific surface area (up by 1.6 times) and higher electron mobility compared to original 1T MoS₂, leading to excellent photo/electrocatalytic HER activity. Impressively, pseudo-1T MoS₂ achieves high visible-light-driven photo-catalytic HER rate of 235.0 mmol·h⁻¹·g⁻¹ in combination with CdS. This work offers an extendable crystal structural fine-tuning approach to promote the catalytic activity of metallic transition metal dichalcogenides.

1. Introduction

Sunlight-driven photocatalytic or electric-driven electrocatalytic water splitting for hydrogen production is regarded as clean and promising approaches to advance solar/electric energy conversion into fuels, in which noble metal platinum (Pt)-based composite photocatalysts or single-component electrocatalyst are commonly used to accelerate hydrogen evolution reaction (HER) and oxygen evolution reaction (OER) by inhibiting the photogenerated electron-hole recombination or minimizing the dynamic overpotentials [1–3]. However, the high cost and scarcity of precious Pt metal promote the production cost of hydrogen from the clean photo/electrocatalytic processes [4]. 2D-layered transition metal dichalcogenides (TMDs) are considered as potential and promising catalysts to substitute noble metal Pt because of their excellent intrinsic catalytic activity and controllable microstructure as well as low price [5,6]. The typical TMDs i.e. MoS₂ has been extensively studied in the catalytic fields, since its edge sites are confirmed to possess near-zero (0.08 eV) hydrogen adsorption free

energy (ΔG_{H^+}) [7,8]. Unfortunately, the conventional MoS₂ is semiconductor 2H phase with a trigonal prismatic structure, and its catalytic activity is severely limited by the scarce edge sites and poor electron mobility [9]. Tuning the crystal structure of 2H MoS₂ for increasing specific surface area has been developed as a typical strategy to enhance its catalytic activity [10–14]. Compared with the high crystalline counterpart, low crystalline 2H MoS₂ exhibits a more disordered structure, larger specific surface area and more accessible active sites, which are favorable for higher catalytic activity. It is worth pointing out that tailoring the crystal structure of 2H MoS₂ can further enhance its catalytic activity to a certain extent, however, the achieved performance is still far from satisfactory, mainly attributed to the inherent shortcomings of 2H MoS₂.

The metallic counterpart i.e. 1T MoS₂ which can be obtained by rotating one of the sulfur plane in 2H MoS₂ by 60° horizontally, exhibits prominent electrical conductivity ca. 10⁷ times higher than that of 2H MoS₂, because of the incompletely filled 4d orbitals of Mo in 1T MoS₂ [15–17]. Except for the edge sites, the basal plane of metallic 1T MoS₂ is

* Corresponding author.

** Corresponding author at: State Key Laboratory of Advanced Metallurgy, University of Science and Technology Beijing, Beijing 100083, PR China.

E-mail addresses: taoxia@mail.buct.edu.cn (X. Tao), yanzhenz@sina.com (Y. Zheng).

¹ These authors contributed equally.

also rich in active sites for HER, favoring a higher reaction kinetics between electrons and protons (H^+) on the basal plane. Benefiting from the above favorable characteristics, 1T MoS_2 can provide a better fundamental and programmable platform to tailor its structure with the aim of achieving high catalytic activity [18,19]. However, it still remains a big challenge to improve the catalytic activity of metastable 1T MoS_2 by modulating its crystal structure, because that its metastable octahedral coordination structure of 1T MoS_2 is inclined to degrade into the low-activity 2H counterpart [20,21]. Most of metallic TMDs including 1T MoS_2 -based electrocatalyst/photocatalyst are prepared from the solution process, in which the precursor residues (e.g., nitrogen species, alkali ions, etc.) could insert in the planes along the *c*-axis [22–25]. Understanding the relationship between intercalated species and metastable metallic structure, and developing a 1T phase non-destructive and lower-crystallinity 1T MoS_2 to enhance the related catalytic activity are very meaningful, however, is yet to report.

In this study, we reveal that the reducible nitrogen-hydrogen species ($-NH$ and $-NH_2$) can affect the lamellar structure of hydrothermally prepared 1T MoS_2 by interlayer Van der Waals force. Understanding this role, we prepare a novel pseudo-1T MoS_2 (P-1T MoS_2) with low crystallinity and less layer thickness by a facile and reproducible H_2O_2 -cleaning strategy to tune the amount of the intercalated $-NH$ and $-NH_2$ species to distort layered structure along *c*-axis direction by weakening the interlayer Van der Waals force. It is found that the P-1T MoS_2 can well accommodate outstanding electronical conductivity, large surface area (up by 1.6 times of 1T MoS_2) together with abundant electrochemically active sites, hence leading to the promoting photo/electrocatalytic performance for water splitting. This work provides a new insight on understanding the role of the intercalated reducible nitrogen-hydrogen species in the crystal structure of metastable 1T MoS_2 , and propose an effective and extendable H_2O_2 -treatment strategy for prepare high-efficient pseudo-1T TMDs catalysts.

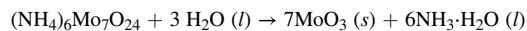
2. Experimental section

2.1. Preparation of 1T MoS_2

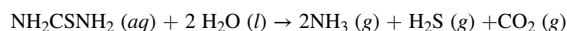
Typically, as shown in Figure S1, $(NH_4)_6Mo_7O_{24} \cdot 4H_2O$ (1.20 g, 0.97

mmol) and NH_2CSNH_2 (2.20 g, 28.90 mmol) were dissolved in deionized water (35 mL), and then form a uniform and transparent solution under vigorous stirring. Subsequently, the solution was added into a Teflon-lined stainless steel autoclave (100 mL) and reacted at 180 °C for 24 h. The reaction equations are as follows:

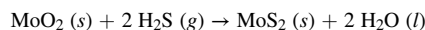
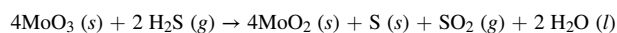
(1) Decomposition of ammonium molybdate:



(2) Decomposition of thiourea:



(3) Reduction and sulfation of molybdenum:



The residual nitrogen-hydrogen species ($-NH_2$ and $-NH$) in 1T MoS_2 may originate from excess and incomplete reaction of thiourea. After cooling to room temperature, the black precipitate was washed several times with deionized water and ethanol by centrifugation. Finally, 1T MoS_2 was obtained by drying overnight at 60 °C under vacuum. It is worth noting that 1T MoS_2 always refers to the product synthesized by $(NH_4)_6Mo_7O_{24} \cdot 4H_2O$ and NH_2CSNH_2 unless otherwise specified.

2.2. Preparation of 1T MoS_2 from precursors without NH_4^+

Typically, Na_2MoO_4 (1.21 g, 5.88 mmol) and NH_2CSNH_2 (1.52 g, 19.97 mmol) were dissolved in deionized water (60 mL). After stirred for 30 min and sonicated for 10 min, the final suspension was transferred into a Teflon-lined autoclave (100 mL) and maintained at 200 °C for 24 h. The precipitate was collected by a centrifuge and washed with distilled water. The final product was obtained after drying under vacuum overnight at 60 °C.

2.3. Preparation of P-1T MoS_2

In a typical process, H_2O_2 solution (50 mM, 20 mL) was prepared in

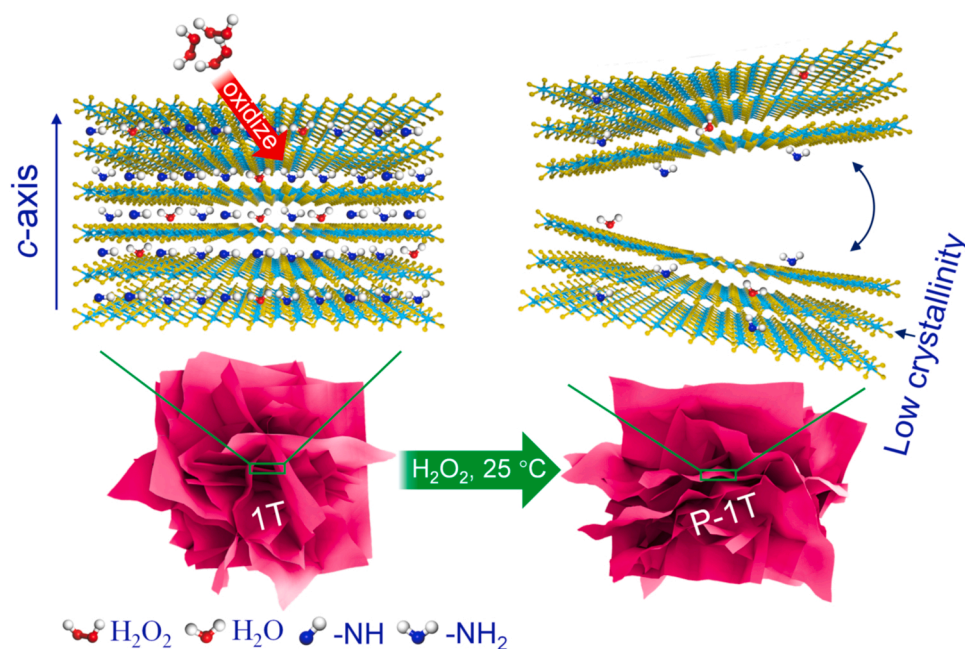


Fig. 1. Schematic illustration for the synthetic procedure of P-1T MoS_2 and the related layer structure along the *c*-axis. The interlayer reducible $-NH$ and $-NH_2$ species in the original 1T MoS_2 are partly removed by H_2O_2 solution, and the interlayer van der Waals force is weakened, which causes the lower crystallinity and reduced layer thickness of P-1T MoS_2 .

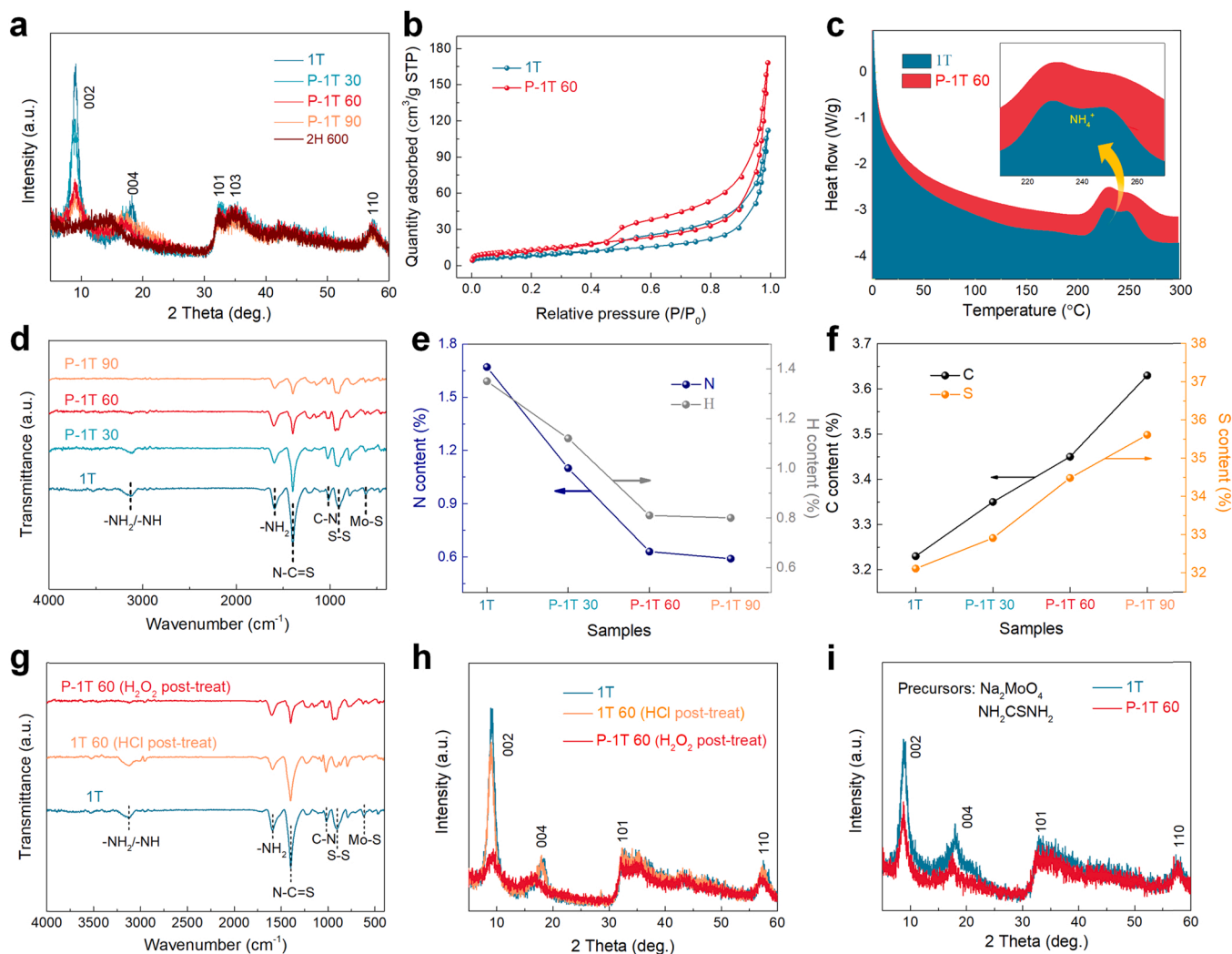


Fig. 2. (a) XRD patterns, (b) N_2 sorption isotherms, (c) DSC curves, (d) FT-IR spectra and (e, f) N, H, C, and S elements quantitative analysis of the samples. (g) FT-IR spectra and (h) XRD patterns of 1T MoS_2 , HCl post-treated 1T MoS_2 (1T 60) and H_2O_2 post-treated 1T MoS_2 (P-1T 60). (i) XRD patterns of 1T MoS_2 preparing using the precursors of Na_2MoO_4 and NH_2CSNH_2 , and the corresponding P-1T 60.

advance. Subsequently, 1T MoS_2 (100 mg) was added into the H_2O_2 solution, followed by stirring at 25 °C for a short time. In this process, H_2O_2 can oxidize the reducible $-NH_2$, and the reaction equation may be as follows: $-NH_2 + H_2O_2 \rightarrow -NHOH + H_2O$. Meanwhile, reducible nitrogen-hydrogen specie $-NH$ was also been removed by oxidizing H_2O_2 . After x seconds of the reaction, the solution was immediately transferred into a beaker containing deionized water (500 mL) to terminate the reaction due to the extremely low concentration of H_2O_2 . Immediately afterwards, dump the excess deionized water after standing for tens of seconds. Finally, the black P-1T MoS_2 (denoted as P-1T x, x represents reaction time) was washed with ethanol (about 50 mL), and then dried under vacuum overnight at 60 °C. The preparation process of all catalysts including P-1T 30, P-1T 60, P-1T 90, 2H 600 and HCl (pH = 4.4) treated 1T 60 is as described above except for the reaction time. In addition, the 1T MoS_2 prepared by Na_2MoO_4 and NH_2CSNH_2 as precursors was also reacted in H_2O_2 solution (50 mM, 20 mL) for 60 s to synthesize the corresponding P-1T 60.

2.4. Preparation of CdS

Specifically, $CdCl_2 \cdot 2.5 H_2O$ (4.60 g, 20.14 mmol) and NH_2CSNH_2 (4.60 g, 60.43 mmol) were added into a Teflon-lined, stainless-steel autoclave filled with ethylenediamine to 60% of its capacity (100 mL).

The autoclave was sealed and heated in an oven at 160 °C for 48 h and then allowed to cool down to room temperature. The yellow precipitate was collected and washed with absolute ethanol and distilled water to remove the solvent residues.

2.5. Preparation of P-1T 60/CdS photocatalyst

As shown in Figure S2, the P-1T 60/CdS photocatalyst was prepared by ultrasonic mixing. In a typical preparation process, CdS (100 mg) and P-1T 60 (20 mg) were added into deionized water (50 mL), followed by sonication for 1 h. Subsequently, the formed precipitate was centrifuged, and then dried at 60 °C under vacuum to obtain the 20 wt% P-1T 60/CdS photocatalyst. Similarly, other P-1T 60/CdS photocatalysts with different ratios (10 wt%, 15 wt%, 25 wt%, 30 wt%) have the same preparation process as 20 wt% P-1T 60/CdS except for the different amount of P-1T 60. In addition, the 3 wt% Pt/CdS was prepared by a in-situ photodeposition process using $H_2PtCl_6 \cdot 6H_2O$. A series of 1T/CdS, P-1T 30/CdS and P-1T 90/CdS were prepared by the same process as P-1T 60/CdS.

3. Results and discussion

3.1. Synthesis and properties of P-1T MoS₂

The removal of intercalated layered-structure-related reducible nitrogen-hydrogen species ($-NH_2$ and $-NH$) by H_2O_2 -treatment is expected to induce changes in the interaction between adjacent 1T MoS₂ layers. Experimentally, P-1T MoS₂ was prepared through a moderate and controllable H_2O_2 -cleaning process, as schematically shown in Fig. 1. Firstly, original 1T MoS₂ was synthesized by hydrothermal process at 180 °C for 24 h (Figure S1). During this process, the two precursors ($(NH_4)_6Mo_7O_{24} \cdot 4H_2O$ and NH_2CSNH_2) were decomposed to form 1T MoS₂ under high temperature and pressure, and the residual nitrogen-hydrogen species such as reducible $-NH$ and $-NH_2$ inevitably remained in the layered structure of 1T MoS₂ (Equation 1&2). Secondly, the 1T MoS₂ was added in a H_2O_2 solution under stirring at 25 °C for a short time, and finally transferred in deionized water to terminate the reaction. Specifically, the interlayer reducible $-NH$ and $-NH_2$ species in the original 1T MoS₂ can be partly removed by the oxidizing HO_2^- and O_2^{2-} in H_2O_2 solution, and the weakening interlayer van der Waals force is expected to cause the orientation deformation (lower crystallinity and less layer thickness) of the layer structure along the c -axis in P-1T MoS₂. Theoretical calculations were performed to explain the interaction between reducible nitrogen-hydrogen species ($-NH_2$ and $-NH$) and MoS₂. The structural models of 1T MoS₂ and P-1T MoS₂ are shown in Figure S3. The separation energy (E_s) on the 1T MoS₂ and P-1T MoS₂ is calculated to evaluate the impact of removing nitrogen-hydrogen species on the lamellar structure of 1T MoS₂ (see Equation S7). The separation energy of 1T MoS₂ and P-1T MoS₂ is calculated as 0.16 eV and 0.06 eV, respectively (Table S1). The removal of interlayer nitrogen-hydrogen species reduces the separation energy between adjacent 1T MoS₂ layers, which is tend to lower its crystallinity as well as reduce the layer thickness.

H_2O_2 concentration and reaction time are the key factors to control the reaction only occurring on the surface nitrogen-hydrogen species of original 1T MoS₂ without causing the degradation of 1T phase into low-activity 2H phase. XRD pattern (Fig. 2a) shows that the (002) diffraction peak position of 1T MoS₂ is located at 9.0°, which is lower than that of 2H MoS₂ (about 14.0°), indicating that the layer spacing of 1T MoS₂ is larger than that of 2H MoS₂. The increased layer spacing of 1T MoS₂ is owing to the embedded nitrogen-containing groups ($-NH_2$ and $-NH$). Besides, the XRD observation (Figure S5) shows that the 1T MoS₂ treated in the 50 mM H_2O_2 for 60 s can maintain metallic phase, and higher concentration of H_2O_2 results in the degradation of 1T to-2H. Thus, we select the 50 mM H_2O_2 solution for the further oxidation period optimization. The original 1T MoS₂ was treated by 50 mM H_2O_2 for 30 s, 60 s, 90 s and 600 s, respectively. Fig. 2a shows that the (002) characteristic peak of 1T phase can be found only in P-1T 30, P-1T 60 and P-1T 90. A new (002) characteristic peak (14.1°) of 2H phase appears in the 2H 600. Raman spectra also give similar phase change information concerning the 2H 600 sample (Figure S6). This means the degradation of original 1T phase into 2H counterpart in the long-term (600 s) exposure to the oxidizing H_2O_2 solution [26]. As for all the P-1T MoS₂ samples (P-1T 30, P-1T 60 and P-1T 90), the degree of crystallinity gradually decreases, as demonstrated by the remarkable time-dependent decrease of the (002) peak by contrast to the original 1T MoS₂ (Fig. 2a). Meanwhile, the obvious increase of half-peak width of the (002) peak indicates that the layer thickness in P-1T MoS₂ samples is decreased [27, 28], attributed to the weakening interlayer van der Waals force inducing by the partial removal of interlayer species. It is noteworthy that after H_2O_2 -treatment, the (002) peak does not negatively shift, indicating that the interlayer spacing (calculated as 0.98 nm based on $2d\sin\theta = n\lambda$) of P-1T MoS₂ samples does not alter. Thus, the fine-tuning of interlayer van der Waals force by controlling the H_2O_2 concentration and reaction time can only disorder the stack of layer along the c -axis direction without changing the interlayer spacing between adjacent MoS₂ layers.

Interestingly, the partial magnification observation of XRD patterns (Figure S7) shows that the c -axis-related (004) peaks of a series of P-1T MoS₂ samples all slightly negatively shift relative to original 1T MoS₂, indicating that (004) crystal lattices still expand even though the typical adjacent (002) lattice spacing does not increase. This is probably owing to the limited reduce of interlayer van der Waals force of original 1T MoS₂, leading to its long-range disorder and short-range order. The crystal structure change from high crystallinity to low crystallinity induced by H_2O_2 -treatment results in the obvious increase of BET specific surface area from $\sim 29.43 \text{ m}^2/\text{g}$ (1T) to $\sim 47.09 \text{ m}^2/\text{g}$ (P-1T 60) (Fig. 2b). Barrett-Joyner-Halenda (BJH) pore size distribution curves (Figure S8) show that the P-1T 60 has a rich microporous structure compared to original 1T sample [29]. Besides, except for the negative shift of the (004) peak and the remarkable time-dependent decrease of the (002) peak, the peak intensity of other characteristic peaks (such as (101), (103) and (110)) in P-1T MoS₂ samples has no significant change. These observations indicate that the partial removal of intercalated layered-structure-related reducible nitrogen-hydrogen species by H_2O_2 -treatment can only change the (002) and (004) crystal planes along the c -axis direction in P-1T MoS₂ samples.

The differential scanning calorimeter (DSC) measurement (Fig. 2c) provides relevant information about intercalated substances. Specifically, the two curves show a downward trend below 200 °C, attributed to the heat absorption of H_2O in the original 1T MoS₂ and P-1T 60. There is no obvious endothermic peak at around 100 °C, indicating that the two samples do not contain NH_3 [24]. A broad exothermic peak appears in the range of 205–275 °C, suggesting that the two samples undergo an irreversible phase transition from the metallic 1T phase to the semiconductor 2H-phase under the nitrogen atmosphere. Note that a faint endothermic peak attributed to NH_4^+ is observed at about 240 °C, indicating the presence of extremely small amounts of NH_4^+ in the two samples [30]. FT-IR spectra (Fig. 2d) shows a absorption band of 3130 cm^{-1} attributed to $-NH$ and/or $-NH_2$ stretching vibrations in the original 1T MoS₂ [31]. This absorption band weakens in P-1T 30 and completely disappears in the remaining samples, due to the gradual removal of nitrogen-hydrogen species by H_2O_2 with increasing treating periods. The FT-IR peaks at 1600 cm^{-1} and 1025 cm^{-1} are assigned to $-NH_2$ variable angle vibration and C-N stretching vibration, respectively [52]. The observed strong peak at 1400 cm^{-1} in the original 1T MoS₂ originates from $N-C=S$ of NH_2CSNH_2 or NH_4^+ of $(NH_4)_6Mo_7O_{24} \cdot 4H_2O$, according to previous reports and the FT-IR characterization (Figure S9) of the two precursors [32–35]. Based on the DSC curve shown in Fig. 2c, the content of NH_4^+ in the samples is extremely small. Therefore, we speculate that the peak at around 1400 cm^{-1} in Fig. 2d mainly originates from the $N-C=S$ stretching vibrational mode. Additionally, one can also observe a decrease in the peak intensities of the $-NH_2$ variable angle vibration, the $N-C=S$ stretching vibration, and the C-N stretching vibration, which is attributed to the removal of nitrogen-containing groups ($-NH_2$ and $-NH$) by H_2O_2 . This has been confirmed by the gradual decrease in the content of N and H elements and the relative increase in the content of C and S elements shown by quantitative analysis (Fig. 2e&f). Consequently, the FT-IR characterization proves that nitrogen-hydrogen groups are partially removed after the H_2O_2 post-treatment process. It is worth noting that the decreasing trend of $-NH_2$ and $-NH$ peak intensity in these samples with prolonging H_2O_2 treating period is similar to the XRD results, confirming the effectiveness of controllably altering intercalated reducible nitrogen-hydrogen species by delicately tuning the concentration and reaction time of H_2O_2 . Besides, the part of the reducible nitrogen-hydrogen species may be oxidized to other functional groups in P-1T 60. After carefully checking, we found a new peak appearing between $1050 \sim 1160 \text{ cm}^{-1}$ in P-1T 60, probably originating from the NO^- and $N_2O_2^{2-}$ species formed by the oxidation of nitrogen-hydrogen species by H_2O_2 [53]. We can also observe a splitting of the S-S peak at 940 cm^{-1} in P-1T 60, which may stem from the interference of H_2O_2 with the residual S matter. Besides, the peaks around 600 cm^{-1} , 900 cm^{-1} , and 1600 cm^{-1} should be

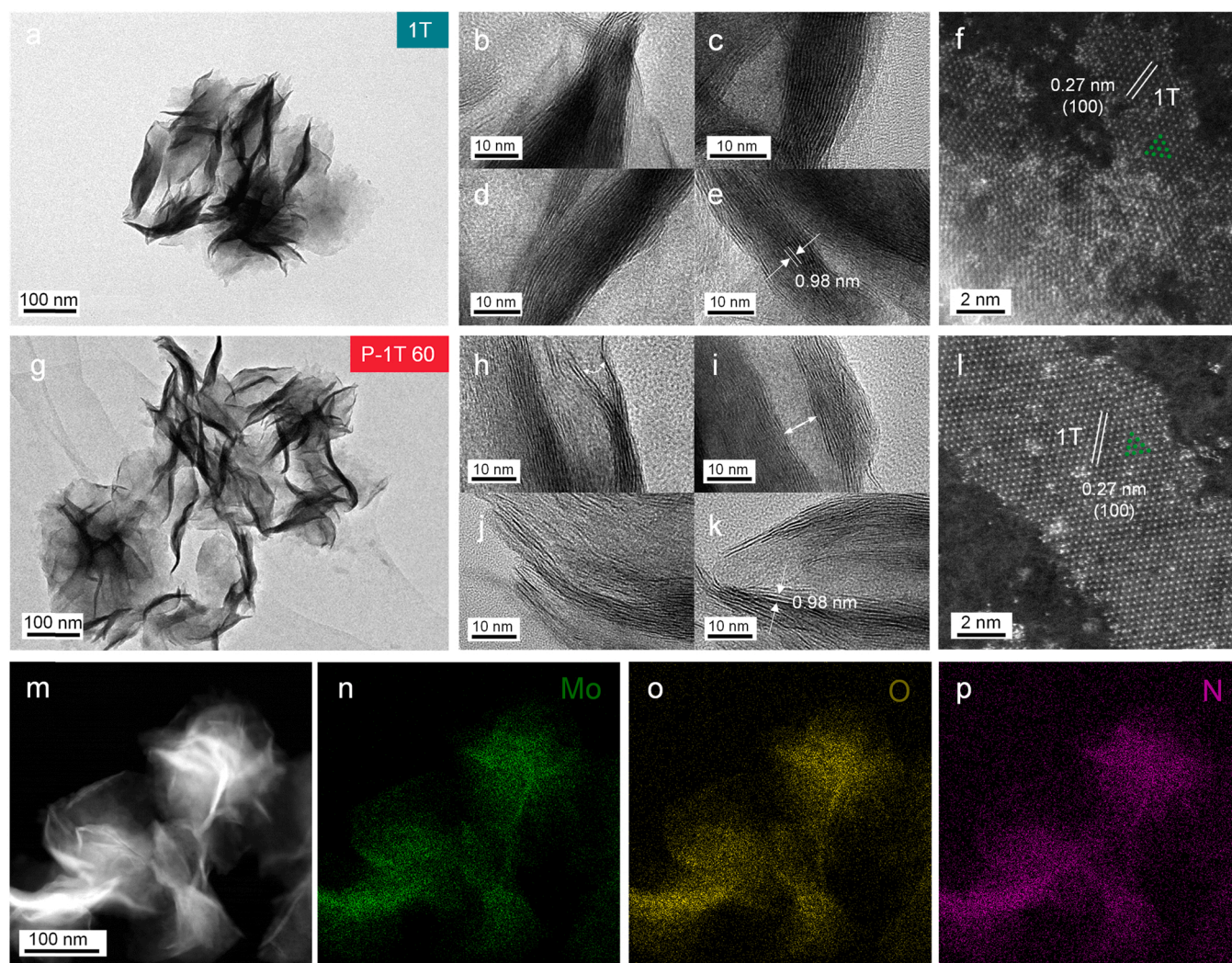


Fig. 3. Microstructure characterizations of 1T MoS₂ and P-1T 60 nanosheets. HRTEM images of (a-e) 1T MoS₂. Top-view HAADF-STEM image of (f) 1T MoS₂. HRTEM images of (g-k) P-1T 60. Top-view HAADF-STEM image of (l) P-1T 60. STEM-EDS mappings of (m-p) P-1T 60.

attributed to Mo-S, S-S and C=O absorption bands, respectively [36–38]. The zeta potential measurement indicates that the removal of uncharged neutral nitrogen-hydrogen species has no effect on the surface charge of these samples (Figure S10).

In order to further understand the mechanism of H₂O₂-cleaning reducible nitrogen-hydrogen species in original 1T MoS₂, an HCl solution with the same H⁺ ion concentration (pH=4.4) as 50 mM H₂O₂ was also used to treat 1T MoS₂ through a similar experimental process. It can be found that the 1T 60 obtained by HCl-treatment exhibits almost the same FT-IR spectra and XRD pattern as original 1T MoS₂, indicating that HCl cannot remove the reducible nitrogen-hydrogen species in 1T MoS₂ (Fig. 2g&h). Besides, the new FT-IR peaks at 1070 cm⁻¹ and 860 cm⁻¹ for HCl-treated 1T 60 are thought to possibly originate from the influence of HCl on 1T MoS₂ to form C-Cl or/and other Cl-containing groups. As shown in Figure S11, Mo, S, O, and N elements are uniformly distributed in the basal plane and edges of both 1T MoS₂ and HCl-treated 1T 60. Note that the content of N element in the HCl-treated 1T 60 (14.60%) is slightly lower than that of the original 1T MoS₂ (16.81%) (Table S2). We speculate that Only slightly reduced (002) characteristic peak of HCl-treated 1T 60 may be due to the inevitably deintercalation of intercalated species during the cleaning process with deionized water and ethanol. Nevertheless, the crystallinity of H₂O₂-treated P-1T 60 is much lower than that of HCl-treated 1T 60. These observations indicate that the partial removal of reducible nitrogen-hydrogen species in

original 1T MoS₂ is independent of H⁺ ions, which is attributed to the oxidizing HO₂⁻ and O₂²⁻ in the H₂O₂ solution. In addition, we also synthesized 1T MoS₂ with NH₄⁺-free precursors (namely Na₂MoO₄ and NH₂CSNH₂), and used H₂O₂ to treat this 1T MoS₂ to verify that the structure evolution is independent of NH₄⁺ (see the Experimental Section for details). As shown in Fig. 2i, the 1T MoS₂ synthesized by the two precursors without NH₄⁺ also shows a significant decrease in crystallinity after H₂O₂-treatment. FT-IR characterization (Figure S12) shows a similar phenomenon i.e. the disappearance of -NH peak at 3130 cm⁻¹ and the decrease of -NH₂ peak at 1400 cm⁻¹. Therefore, we can infer that -NH and -NH₂ in P-1T 60 are derived from the precursor NH₂CSNH₂ instead of (NH₄)₆Mo₇O₂₄·4H₂O, and the structure evolution originates from the removal of reducible -NH and -NH₂. More importantly, this investigation indicates that the H₂O₂-cleaning method we developed is also effective on the other catalysts with similar reducible nitrogen-hydrogen species, which is conducive to their performance optimization.

X-ray photoelectron spectroscopy show that the percentage of 2H MoS₂ is almost the same in 1T MoS₂ (19.5%) and P-1T 60 (21.8%) (Figure S13 and Table S3), thus, we do not consider the effect of 2H phase on the catalytic activity of these two samples. Besides, although both 1T MoS₂ and P-1T 60 show strong Mo-O bond in XPS, the intensity of Mo-O bond in P-1T 60 is not stronger than that of original 1T MoS₂ (Figure S13a&i). Thus, we believe that H₂O₂ can not oxidize MoS₂. The

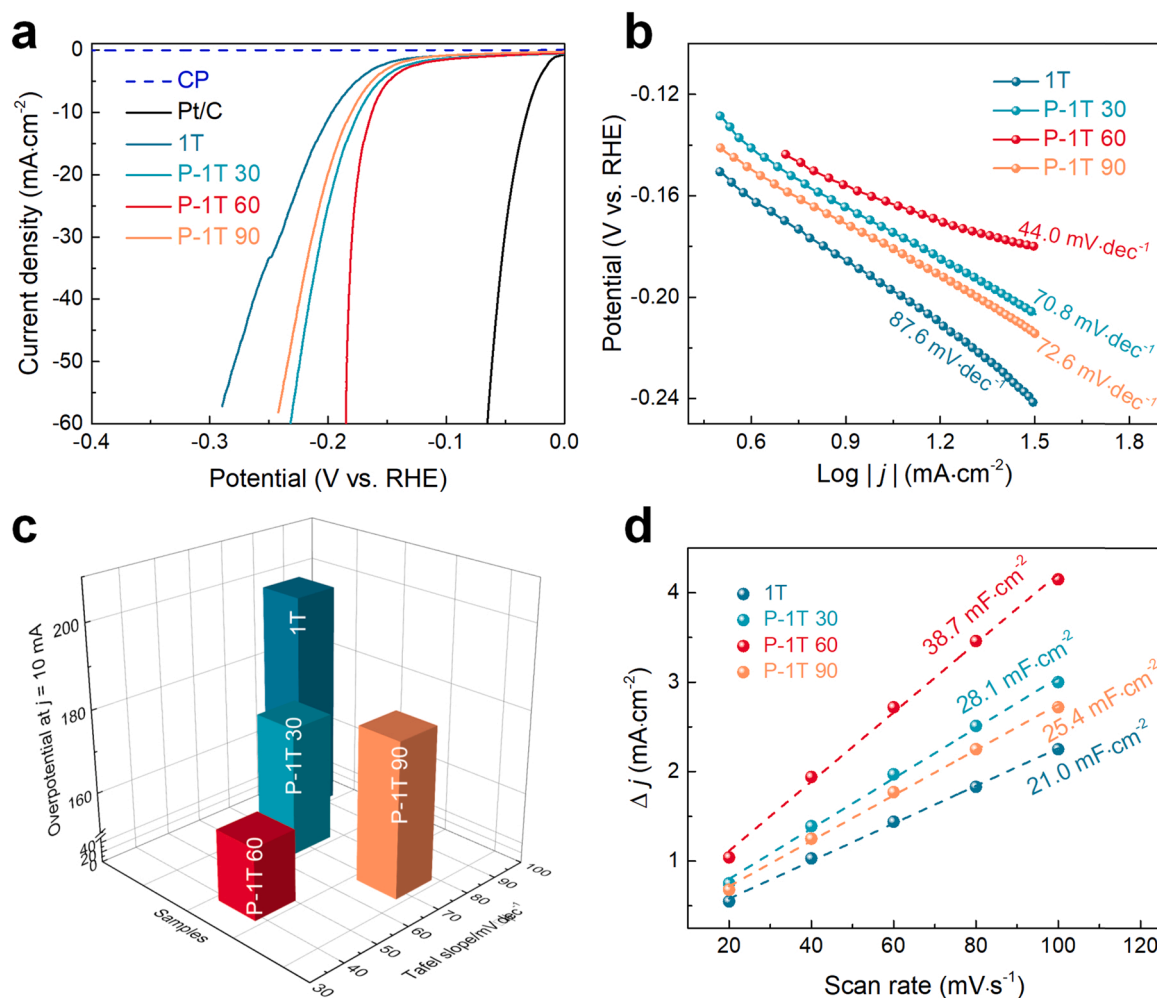


Fig. 4. Electrochemical performances of 1T MoS₂ and P-1T MoS₂ (including P-1T 30, P-1T 60 and P-1T 90). (a) Polarization curves, (b) Tafel slopes, (c) performance comparison, (d) C_{dl} values.

N 1 s spectra reveal that these four samples do not contain NH₄⁺, which is consistent with the DSC characterization (Fig. 2c) [39]. Nevertheless, the high-resolution XPS analysis still reveals a gradual decrease trend of the content of N element in the four samples (Table S3), further confirming the H₂O₂-removal effect on reducible -NH and -NH₂ species. SEM images clearly reveal that P-1T 60 displays a flower-like structure composed of nanosheets similar to original 1T MoS₂ (Figure S14). As expected, the H₂O₂-treatment does not cause serious discernable structural damage to P-1T 60. The ultrathin lamellar structure with a lateral size of about 200–300 nanometers endows P-1T 60 with a wealth of accessible edges and basal active sites [40]. Besides, the EDS analysis attached to the SEM show that N, O, Mo, S elements are evenly distributed in 1T MoS₂ and P-1T 60 (Figure S15 & S16), and the N element drops from 1.34% in 1T MoS₂ to 1.12% in P-1T 60. This downward trend is similar to the result of XPS analysis (Table S3). The different results presented by the two detection methods (XPS and EDS) regarding element content may be due to their different detection ranges and depths.

High-resolution transmission electron microscopy (HRTEM) provides the detailed microstructure and phase-related information of 1T MoS₂ and P-1T 60. Both 1T MoS₂ and P-1T 60 are corrugated graphene-like nanoflowers composed of several nanosheets (Fig. 3a&g). The wide-field TEM images exhibit that the microstructures of 1T MoS₂ and P-1T 60 are not significantly different. The regular and thick layered structure are observed in the magnified cross-sectional HRTEM images of nanosheet with respect to the (002) crystal planes of 1T MoS₂ (Fig. 3b-e). The

interplanar spacing of (002) planes is measured to be approximately 0.98 nm in Fig. 3e, which is consistent with the result of XRD characterization [12,41]. Interestingly, the layered structure of P-1T 60 is somewhat disordered with lower crystallinity and less layer thickness (Fig. 3h-k). Thus, the partial removal of reducible -NH and -NH₂ species weakens the interlayer van der Waals force, resulting in the distortion of the layered structure of P-1T 60, which is conducive to the exposure of more active sites. The (002) lattice spacing with 0.98 nm of P-1T 60 (Fig. 3k) is similar to that of 1T MoS₂, which is consistent with the observation that the (002) peak does not negatively shift significantly in the XRD patterns (Fig. 2a). We have carried out HAADF-STEM characterization of the samples to identify the 1T phase MoS₂. As shown in the Fig. 3f&l, the characteristic crystalline lattice structure of the 1T phase in 1T MoS₂ and P-1T 60 is confirmed. Both samples show Mo-S octahedral coordination with a lattice spacing of 0.27 nm, corresponding to the (100) plane of the 1T phase [51]. Mo, O, and N elements are uniformly distributed in the basal plane and edges of P-1T 60 (Fig. 3m-p). Meanwhile, as shown in the Figure S17, we also observe a typical honeycomb arrangement of atoms belonging to the 2H phase on P-1T 90, which is distinctly different from the 1T phase. Consequently, the structure of 1T phase MoS₂ can be confirmed by HAADF-STEM. Such observations indicate that the moderate H₂O₂-treatment does not cause degradation of the surface atomic structure of the P-1T 60.

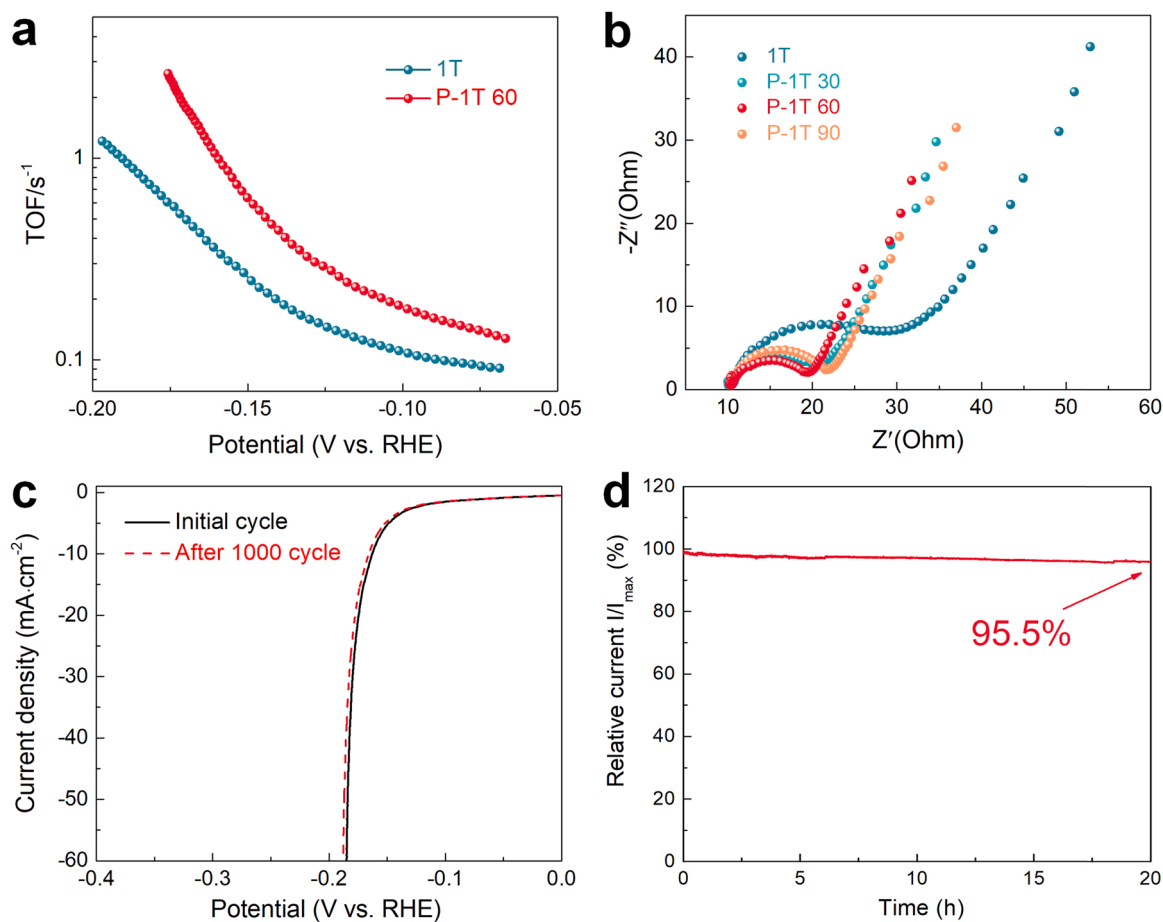


Fig. 5. (a) TOF curves of 1T MoS₂ and P-1T 60. (b) EIS plots of 1T MoS₂, P-1T 30, P-1T 60 and P-1T 90. (c) Cycling stability and (d) Chronoamperometry curve of P-1T 60 for HER in 0.5 M H₂SO₄.

3.2. Electrocatalytic HER performance

Firstly, we evaluated the development of the catalytic activity of the S-active site of basal plane after removing part of nitrogen-hydrogen species (-NH₂ and -NH). The catalytic HER performance on S-active site can be evaluated via calculating the reaction free energy for hydrogen adsorption (ΔG_{H^*}), which is determined as Equation S8. As expected, the ΔG_{H^*} calculated on the S-active site of basal plane is 1.5 eV for 1T MoS₂, which is dramatically reduced to 0.7 eV for P-1T MoS₂ (Figure S4). This reduce in ΔG_{H^*} implies that the intrinsic catalytic HER activity of the S-active site on the P-1T MoS₂ basal plane is enhanced by the removal of part of the nitrogen-hydrogen species. Besides, we can speculate that the surface species would affect the basal S-active site and intrinsic catalytic activity as a consequence. To verify the electrocatalytic performance, the samples were experimentally characterized by electrochemical measurements in Ar-saturated 0.5 M H₂SO₄ solution using a three-electrode device with a mass load of 0.4 mg cm⁻² on the carbon paper (CP) working electrode. Fig. 4a displays the LSV curves of CP, 1T MoS₂, three P-1T MoS₂ samples and commercial Pt/C at the scan rate of 5 mV s⁻¹. Through standard calibration, all potentials presented here are referenced to the reversible hydrogen electrode (RHE) [39]. Obviously, the three P-1T MoS₂ samples show significantly increased catalytic activity compared to original 1T MoS₂, which is attributed to the favorable transformation of the crystal structure caused by the partial removal of reducible nitrogen-hydrogen species. Among them, P-1T 60 achieves the best HER performance, with only 165 mV overpotential to reach 10 mA cm⁻² (η_{10}) owing to the cathodic current rises rapidly under more negative potentials [42]. The corresponding Tafel slopes were investigated to evaluate the kinetic reaction mechanism of

the samples as shown in Fig. 4b. The resulting Tafel slope of P-1 T 60 is 44.0 mV dec⁻¹, whereas 1T MoS₂, P-1T 30, and P-1T 90 possess much higher values of 87.6, 70.8, and 72.6 mV dec⁻¹, respectively. Such a low Tafel slope suggests that P-1T 60 undergoes a favorable Volmer-Heyrovsky mechanism for HER and is advantageous for practical applications because the faster increase of HER rate with increasing overpotential [19]. Meanwhile, Fig. 4c & Table S4 show that P-1T 60 has significant advantages over other catalysts in terms of overpotential and Tafel slope parameters.

The electrochemical surface area (ECSA) values were measured by double-layer capacitance (C_{dl}) [19]. For the prepared electrocatalysts, their C_{dl} values were obtained by cyclic voltammetry (CV) at the scan rate of 20–100 mV s⁻¹ under a narrow potential window (Figure S18). As shown in Fig. 4d, the C_{dl} value of P-1T 60 is calculated to be 38.7 mF cm⁻², which is much higher than that of 1T MoS₂ (21.0 mF cm⁻²), P-1T 30 (28.1 mF cm⁻²) and P-1T 90 (25.4 mF cm⁻²). Furthermore, the ECSA values of the samples are determined based on their C_{dl} values. As expected, P-1T 60 possesses the larger ECSA value of 967.5 cm²_{ECSA} compared to other samples, confirming its more accessible active sites [9]. According to the previous analysis, the increased ECSA value of P-1T 60 is attributed to the low crystallinity and less layer thickness caused by the H₂O₂-treatment. Additionally, the LSV curves of the samples normalized by their ECSA values (Figure S19) display that P-1T 60 has the highest catalytic performance for HER with regard to the ECSA, suggesting its excellent intrinsic catalytic activity [43]. Meanwhile, based on these CV measurements (Figure S20), the hydrogen turnover frequency (TOF) curve of P-1T 60 is significantly higher than that of 1T MoS₂ as shown in Fig. 5a. Associated with above analysis, the prepared P-1T 60 possesses higher intrinsic activity than original 1T

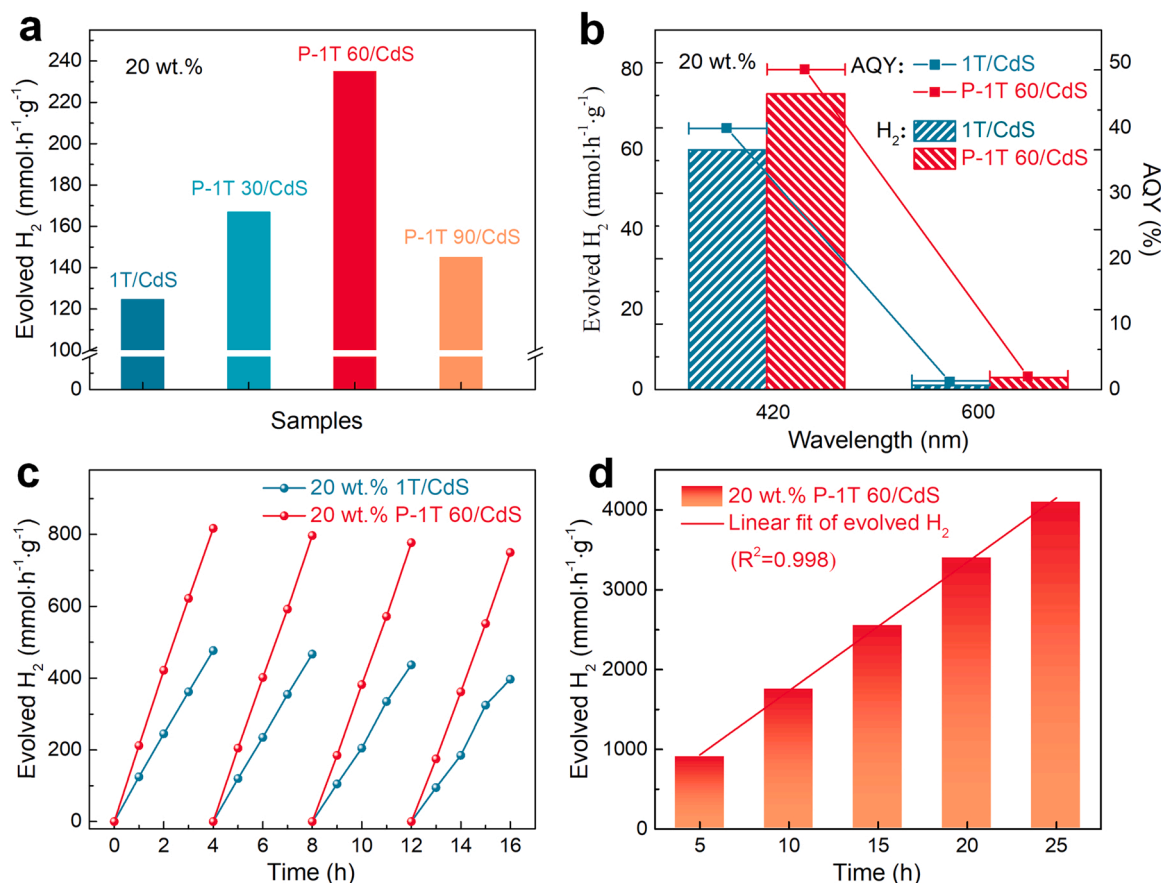


Fig. 6. (a) Photocatalytic performance of photocatalysts under 20 wt% loading amount of 1T MoS₂ or P-1T MoS₂ (including P-1T 30, P-1T 60 and P-1T 90) under visible light. (b) AQY values and HER rates of 20 wt% 1T/CdS and 20 wt% P-1T 60/CdS at 420 nm and 600 nm wavelength. (c) Cyclic photocatalytic HER on 20 wt% P-1T 60/CdS and 20 wt% 1T/CdS. (d) Photocatalytic HER catalyzed by 20 wt% P-1T 60/CdS under a prolonged visible light irradiation of 25 h.

MoS₂. Nyquist diagram exhibits a smallest semicircle for P-1T 60 among all the tested electrodes (Fig. 5b), indicating that P-1T 60 possesses the lowest charge transfer resistance (R_{ct}) at the electrode-electrolyte interface. The smallest R_{ct} value means the highest conductivity of P-1T 60 compared to other prepared catalysts. Of course, a potential electrocatalyst is expected to exhibit excellent durability and structural stability. The stability of P-1T 60 performed by continuous CV scanning at a scan rate of 50 mV·s⁻¹ does not weaken obviously (Fig. 5c). The chronoamperometry measurement also confirmed the excellent stability of P-1T 60 during the 20 h HER process (Fig. 5d). The SEM (Figure S21a&c) and HRTEM (Figure S21b&d) images of the used P-1T 60 electrocatalyst after continuous CV test further demonstrate its structure stability.

3.3. Photocatalytic HER performance

Our previous studies have shown that MoS₂-based catalysts with excellent electrocatalytic activity generally perform prominent in photocatalytic field as cocatalyst [40,44]. Here, P-1T 60 is combined with the commonly used CdS to construct composite photocatalyst (Figure S22) for evaluating the photocatalytic performance. The EDS mappings (Figure S23 & S24) also show the successful formation of the compact P-1T 60/CdS heterojunction because Mo, S, O, N and Cd elements are uniformly distributed in their compounds. Compared to pure CdS, 20 wt% P-1T 60/CdS displays similar absorption edge but higher adsorption strength, which is beneficial to the photocatalytic hydrogen evolution activity (Figure S25). The photocatalytic HER rates of the samples was measured under visible light irradiation ($\lambda > 420$ nm) with lactic acid (LA) as sacrificial reagent. LA is an electron donor, and the

role of LA in photocatalytic HER is to efficiently consume h^+ , thus facilitating the photogenerated e^- to react rapidly with electron acceptor i.e. H₂O to produce H₂. Fig. 6a and Figure S26 shows that the photocatalytic HER rate achieves up to 235.0 mmol·h⁻¹·g⁻¹ for P-1T 60/CdS at the optimal level at 20 wt%. Such a remarkably high HER activity exceeds that of Pt/CdS (104.5 mmol·h⁻¹·g⁻¹), 1T/CdS (124.7 mmol·h⁻¹·g⁻¹), P-1T 30/CdS (167.0 mmol·h⁻¹·g⁻¹), P-1T 90/CdS (145.0 mmol·h⁻¹·g⁻¹) as well as the previously reported highest visible-light-driven HER performance of MoS₂/CdS photocatalytic systems (Table S5), which is attributed to the excellent intrinsic structure of P-1T 60 with the increased specific surface area, accessible active sites and excellent electron mobility. Besides, the AQY values of 20 wt% P-1T 60/CdS (49.0% at 420 nm and 2.0% at 600 nm) are higher than that of 1T/CdS (40.0% at 420 nm and 1.2% at 600 nm) (Fig. 6b). Furthermore, 20 wt% P-1T 60/CdS shows obvious UV-vis absorption-dependent AQY values in the wide range of monochromatic wavelengths (Figure S27). The stability assays (Fig. 6c) show that 20 wt% P-1T 60/CdS and 20 wt% 1T/CdS both possess good catalytic stability after four runs and the photocatalytic HER activity of the former is obviously higher than that of the latter. Almost no obvious attenuation within 25 h under a prolonged visible light irradiation ($\lambda > 420$ nm) further confirms the good stability of 20 wt% P-1T 60/CdS (Fig. 6d).

The polarization curves (Fig. 7a) exhibit that 20 wt% P-1T 60/CdS has higher current density than pure CdS and 20 wt% 1T/CdS. Fig. 7b shows a typical Nyquist plot with the smallest diameter of 20 wt% P-1T 60/CdS under light illumination, indicating efficient interfacial charge transfer in 20 wt% P-1T 60/CdS heterostructure [45]. Meanwhile, the high photocurrent response intensity of 20 wt% P-1T 60/CdS in transient photocurrent responses suggests that P-1T 60 greatly promotes the

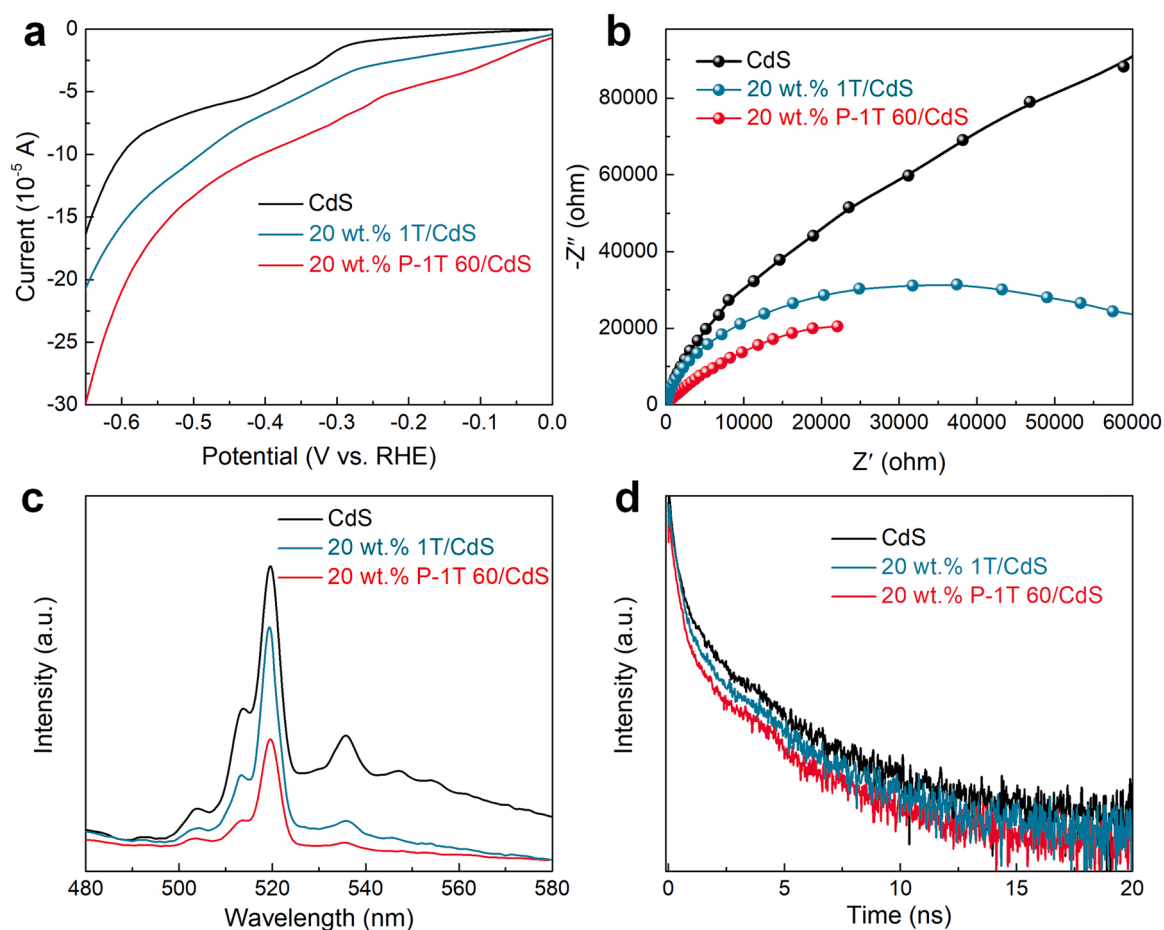


Fig. 7. (a) Polarization curves, (b) EIS Nyquist plots, (c) PL and (d) TRPL spectra of CdS, 20 wt.% 1T/CdS and 20 wt.% P-1T 60/CdS.

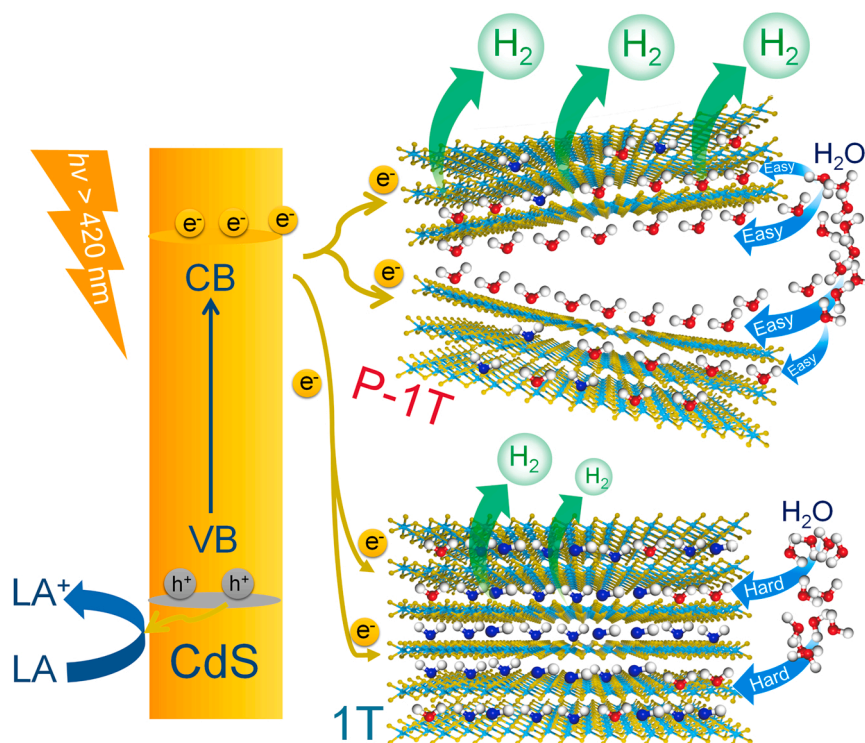


Fig. 8. Schematic diagram of photogenerated electron transfer from CdS to P-1T MoS₂ (or 1T MoS₂) and diffusion of water molecules to the active sites for hydrogen evolution.

transport and separation of photogenerated carriers on CdS (Figure S28) [46]. Based on above photoelectrochemical tests, the best photocatalytic activity of 20 wt% P-1T 60/CdS can be attributed to its higher carrier separation efficiency and lower charge transport resistance which is related to high-percent metallic phase and low-dose nitrogen-hydrogen species within the interlayer.

UV–vis diffuse-reflectance spectra (Figure S29) reveal the metallic characteristics of 1T MoS₂, P-1T 30, P-1T 60, and P-1T 90 with no obvious absorption edge [47]. PL spectrum (Fig. 7c) was used to evaluate the recombination of photogenerated electron-hole pairs. The broad fluorescence peak at about 519 nm in all samples with various P-1T 60 loading content can be attributed to the near-band edge emission of CdS [48]. The peak at ~536 nm is related to structural defects on the surface of the CdS nanorods. Due to the high recombination of photogenerated carriers, pure CdS shows the strongest emission. As expected, 20 wt% P-1T 60/CdS shows the lowest PL intensity owing to the rapid electron transfer from CdS to P-1T 60, hence leading to inhibited carrier recombination and best HER activity. A lower PL peak intensity indicates the more efficient carrier separation, and this also corresponds to a shorter PL lifetime for transfer the e^- from the CdS to the cocatalyst. Furthermore, the time-resolved photoluminescence (TRPL) measurement was also applied to evaluate the transfer of photogenerated electrons in the samples by quantitatively calculation of decay lifetime. Fig. 7d & Table S6 exhibits that the average decay lifetimes are calculated to be 2.41 ns for pure CdS, 1.89 ns for 20 wt% 1T/CdS and 1.48 ns for 20 wt% P-1T 60/CdS, respectively. The lowest PL lifetime indicates that the electrons are quickly transferred from CdS to P-1T 60, and electron-hole separation is effectively promoted in the 20 wt% P-1T 60/CdS [49,50].

The photocatalytic working mechanism under visible light ($\lambda > 420$ nm) is illustrated in Fig. 8. P-1T MoS₂ (P-1T 60) and original 1T MoS₂ are loaded on CdS nanorods to extract photogenerated electrons from CdS through different electron transport paths. On the one hand, the layered structure with reduced thickness and low crystallinity endows P-1T MoS₂ with higher BET specific surface area and more active sites. Water molecules are easier to reach the active sites on P-1T MoS₂ than on 1T MoS₂. On the other hand, P-1T MoS₂ has higher conductivity, thus the photogenerated electrons can be transferred faster on P-1T MoS₂ than on 1T MoS₂. Therefore, faster electron transfer and more accessible active sites on P-1T MoS₂ enable the photogenerated electrons from CdS to be efficiently consumed in the reduction reaction of water and lead to efficient hydrogen evolution.

The innovations of P-1T MoS₂ can be summarized into the following points. (1) The P-1T MoS₂ maintains metallic intrinsic structure and large specific surface area, showing the favorable features of excellent electrical conductivity and easily accessible active sites. (2) The P-1T MoS₂ shows a lower reaction free energy for hydrogen adsorption (ΔG_{H^+}) on the basal S-active site than 1T MoS₂, resulting in a higher intrinsic catalytic activity. (3) The P-1T MoS₂ shows excellent electrocatalytic HER activity in acidic media and superior photocatalytic HER activity using as a cocatalyst for commonly used CdS under visible light. For the photocatalytic and electrocatalytic HER process, the positive effects of P-1T MoS₂ on the enhancement of HER performance are almost the same, that is, providing higher electronic conductivity and more accessible reaction sites. Specifically, for the electrocatalytic HER process, P-1T MoS₂ is capable of providing numerous, more accessible, and higher intrinsic activity reaction sites for electrons (e^-) from the external circuit, leading to a more efficient reaction between H^+ in acidic media and e^- at the active site to produce H₂. For photocatalytic HER, the highly conductive P-1T MoS₂ as cocatalyst can rapidly extracts e^- from CdS and then provides numerous, more accessible, and higher intrinsic activity reaction sites for H^+ reduction by e^- .

4. Conclusion

In summary, we developed a moderate and controllable H₂O₂-

cleaning strategy to prepare a novel P-1T MoS₂ (P-1T 60) by distorting layered structure along c-axis orientation of the solution-processing 1T MoS₂. XRD, BET, FT-IR, HRTEM etc. characterizations confirm that the oxidation species in the H₂O₂ solution can remove part of intercalated reducible nitrogen-hydrogen species (-NH and -NH₂) and weaken interlayer Van der Waals force of 1T MoS₂, leading to the less layer thickness and low crystallinity of P-1T MoS₂. As a result, the resultant P-1T MoS₂ exhibits high specific surface area, abundant accessible active sites, and improved conductivity. The P-1T MoS₂ shows excellent electrocatalytic HER activity in acidic media and superior photocatalytic HER activity (235.0 mmol·h⁻¹·g⁻¹) using as a cocatalyst for commonly used CdS under visible light ($\lambda > 420$ nm). This work reveals the key role of reducible nitrogen-hydrogen species in maintaining the crystal structure of metastable 1T MoS₂, and develops a facile structure fine-tuning strategy by a moderate oxidation process.

CRediT authorship contribution statement

Xitao Li: Conceptualization, Methodology, Formal analysis, Investigation, Writing – original draft, Writing – review & editing, Visualization. **Xiangnan Sun:** Formal analysis, Investigation, Validation. **Haifeng Yu:** Formal analysis, Software. **Haotong Li:** Validation. **Xueyi Sun:** Resources. **Xia Tao:** Resources, Supervision, Project administration, Funding acquisition. **YanZhen Zheng:** Conceptualization, Writing – review & editing, Resources, Supervision, Project administration, Funding acquisition.

Declaration of Competing Interest

The authors declare that they have no known competing financial interests or personal relationships that could have appeared to influence the work reported in this paper.

Acknowledgements

The Opening Project of State Key Laboratory of Organic-Inorganic Composites (Nos. oic-202101001).

Appendix A. Supporting information

Supplementary data associated with this article can be found in the online version at doi: 10.1016/j.apcatb.2022.121156.

References

- [1] S. Chen, T. Takata, K. Domen, Particulate photocatalysts for overall water splitting, *Nat. Rev. Mater.* 2 (2017) 17050, <https://doi.org/10.1038/natrevmats.2017.50>.
- [2] X. Lv, X. Li, C. Yang, X. Ding, Y. Zhang, Y.-Z. Zheng, S. Li, X. Sun, X. Tao, Large-size, porous, ultrathin NiCoP nanosheets for efficient electro/photocatalytic water splitting, *Adv. Funct. Mater.* 30 (2020) 1910830, <https://doi.org/10.1002/adfm.201910830>.
- [3] Z.W. Seh, J. Kibsgaard, C. Dickens, I.B. Chorkendorff, J. Nørskov, T. Jaramillo, Combining theory and experiment in electrocatalysis: insights into materials design, *Science* 355 (2017) 6321, <https://doi.org/10.1126/science.aad4998>.
- [4] X. Zou, Y. Zhang, Noble metal-free hydrogen evolution catalysts for water splitting, *Chem. Soc. Rev.* 44 (2015) 5148–5180, <https://doi.org/10.1039/c4cs00448e>.
- [5] D. Voiry, J. Yang, M. Chhowalla, Recent strategies for improving the catalytic activity of 2D TMD nanosheets toward the hydrogen evolution reaction, *Adv. Mater.* 28 (2016) 6197, <https://doi.org/10.1002/adma.201505597>.
- [6] L. Lin, P. Sherrell, Y. Liu, W. Lei, S. Zhang, H. Zhang, G.G. Wallace, J. Chen, Engineered 2D transition metal dichalcogenides-a vision of viable hydrogen evolution reaction catalysis, *Adv. Energy Mater.* 10 (2020) 1903870, <https://doi.org/10.1002/aenm.201903870>.
- [7] B. Hinnemann, P.G. Moses, J. Bonde, K.P. Jørgensen, J.H. Nielsen, S. Hørch, I. Chorkendorff, J.K. Nørskov, Biomimetic hydrogen evolution: MoS₂ nanoparticles as catalyst for hydrogen evolution, *J. Am. Chem. Soc.* 127 (2005) 5308–5309, <https://doi.org/10.1021/ja0504690>.
- [8] T.F. Jaramillo, K.P. Jørgensen, J. Bonde, J.H. Nielsen, S. Hørch, I. Chorkendorff, Identification of active edge sites for electrochemical H₂ evolution from MoS₂ nanocatalysts, *Science* 317 (2007) 100–102, <https://doi.org/10.1126/science.1141483>.

- [9] Q. Fu, J. Han, X. Wang, P. Xu, T. Yao, J. Zhong, W. Zhong, S. Liu, T. Gao, Z. Zhang, L. Xu, B. Song, 2D transition metal dichalcogenides: design, modulation, and challenges in electrocatalysis, *Adv. Mater.* 33 (2021) 1907818, <https://doi.org/10.1002/adma.201907818>.
- [10] H. Sun, X. Ji, Y. Qiu, Y. Zhang, Z. Ma, G.-g. Gao, P. Hu, Poor crystalline MoS₂ with highly exposed active sites for the improved hydrogen evolution reaction performance, *J. Alloy. Compd.* 777 (2019) 514–523, <https://doi.org/10.1016/j.jallcom.2018.10.364>.
- [11] D. Wang, Y. Xie, Z. Wu, Amorphous phosphorus-doped MoS₂ catalyst for efficient hydrogen evolution reaction, *Nanotechnology* 30 (2019), 205401, <https://doi.org/10.1088/1361-6528/aaff2>.
- [12] P. Cao, J. Peng, J. Li, M. Zhai, Highly conductive carbon black supported amorphous molybdenum disulfide for efficient hydrogen evolution reaction, *J. Power Sources* 347 (2017) 210–219, <https://doi.org/10.1016/j.jpowsour.2017.02.056>.
- [13] D. Merki, S. Fierro, H. Vrubel, X. Hu, Amorphous molybdenum sulfide films as catalysts for electrochemical hydrogen production in water, *Chem. Sci.* 2 (2011) 1262–1267, <https://doi.org/10.1039/c1sc00117e>.
- [14] J.D. Benck, Z. Chen, Leah Y. Kuritzky, A.J. Forman, T.F. Jaramillo, Amorphous molybdenum sulfide catalysts for electrochemical hydrogen production: insights into the origin of their catalytic activity, *ACS Catal.* 2 (2012) 1916–1923, <https://doi.org/10.1021/cs300451q>.
- [15] Z. Lei, J. Zhan, L. Tang, Y. Zhang, Y. Wang, Recent development of metallic (1T) phase of molybdenum disulfide for energy conversion and storage, *Adv. Energy Mater.* 8 (2018) 1703482, <https://doi.org/10.1002/aenm.201703482>.
- [16] S. Shi, Z. Sun, Y.H. Hu, Synthesis, stabilization and applications of 2-dimensional 1T metallic MoS₂, *J. Mater. Chem. A* 6 (2018) 23932, <https://doi.org/10.1039/c8ta08152b>.
- [17] D. Sun, D. Huang, H. Wang, G.-L. Xu, X. Zhang, R. Zhang, Y. Tang, D. Abd El-Hady, W. Alshitari, A. Saad Al-Bogami, K. Amine, M. Shao, 1T MoS₂ nanosheets with extraordinary sodium storage properties via thermal-driven ion intercalation assisted exfoliation of bulky MoS₂, *Nano Energy* 61 (2019) 361–369, <https://doi.org/10.1016/j.nanoen.2019.04.063>.
- [18] K. Qi, X. Cui, L. Gu, S. Yu, X. Fan, M. Luo, S. Xu, N. Li, L. Zheng, Q. Zhang, J. Ma, Y. Gong, F. Lv, K. Wang, H. Huang, W. Zhang, S. Guo, W. Zheng, P. Liu, Single-atom cobalt array bound to distorted 1T MoS₂ with ensemble effect for hydrogen evolution catalysis, *Nat. Commun.* 10 (2019) 5231, <https://doi.org/10.1038/s41467-019-12997-7>.
- [19] M.A.R. Anjum, H.Y. Jeong, M.H. Lee, H.S. Shin, J.S. Lee, Efficient hydrogen evolution reaction catalysis in alkaline media by All-in-One MoS₂ with multifunctional active sites, *Adv. Mater.* 30 (2018) 1707105, <https://doi.org/10.1002/adma.201707105>.
- [20] E.E. Benson, H. Zhang, S.A. Schuman, S.U. Nanayakkara, N.D. Bronstein, S. Ferrere, J.L. Blackburn, E.M. Miller, Balancing the hydrogen evolution reaction, surface energetics, and stability of metallic MoS₂ nanosheets via covalent functionalization, *J. Am. Chem. Soc.* 140 (2018) 441–450, <https://doi.org/10.1021/jacs.7b11242>.
- [21] A.S. Goloveshkin, N.D. Lenenko, A.V. Naumkin, A.Y. Pereyaslavtsev, A. V. Grigorieva, A.V. Shapovalov, V.N. Talanova, A.V. Polezhaev, V.I. Zaikovskii, V. V. Novikov, Enhancement of 1T-MoS₂ superambient temperature stability and hydrogen evolution performance by intercalating a phenanthroline monolayer, *ChemNanoMat* 7 (2021) 447, <https://doi.org/10.1002/cnma.202000586>.
- [22] M.S. Sokolikova, C. Mattevi, Direct synthesis of metastable phases of 2D transition metal dichalcogenides, *Chem. Soc. Rev.* 49 (2020) 3952–3980, <https://doi.org/10.1039/d0cs00143k>.
- [23] I.H. Kwak, I.S. Kwon, H.G. Abbas, G. Jung, Y. Lee, J. Park, H.S. Kang, Stable methylammonium-intercalated 1T'-MoS₂ for efficient electrocatalytic hydrogen evolution, *J. Mater. Chem. A* 6 (2018) 5613–5617, <https://doi.org/10.1039/c8ta00700d>.
- [24] Q. Liu, X. Li, Q. He, A. Khalil, D. Liu, T. Xiang, X. Wu, L. Song, Gram-scale aqueous synthesis of stable few-layered 1T-MoS₂: applications for visible-light-driven photocatalytic hydrogen evolution, *Small* 11 (2015) 5556–5564, <https://doi.org/10.1002/smll.201501822>.
- [25] L. Wu, N.Y. Dzade, M. Yu, B. Mezari, A.J.F. van Hoof, H. Friedrich, N.H. de Leeuw, E.J.M. Hensen, J.P. Hofmann, Unraveling the role of lithium in enhancing the hydrogen evolution activity of MoS₂: intercalation versus adsorption, *ACS Energy Lett.* 4 (2019) 1733–1740, <https://doi.org/10.1021/acsenenergylett.9b00945>.
- [26] K. Chang, X. Hai, H. Pang, H. Zhang, L. Shi, G. Liu, H. Liu, G. Zhao, M. Li, J. Ye, Targeted synthesis of 2H- and 1T-phase MoS₂ monolayers for catalytic hydrogen evolution, *Adv. Mater.* 28 (2016) 10033, <https://doi.org/10.1002/adma.201603765>.
- [27] R. Romero-Rivera, A.G. Camacho, M. Del Valle, G. Alonso, S. Fuentes, J. Cruz-Reyes, HDS of DBT with molybdenum disulfide catalysts prepared by in situ decomposition of alkyltrimethylammonium thiomolybdates, *Top. Catal.* 54 (2011) 561–567, <https://doi.org/10.1007/s12444-011-9620-2>.
- [28] C.B. Ma, X. Qi, B. Chen, S. Bao, Z. Yin, X.J. Wu, Z. Luo, J. Wei, H.L. Zhang, H. Zhang, MoS₂ nanoflower-decorated reduced graphene oxide paper for high-performance hydrogen evolution reaction, *Nanoscale* 6 (2014) 5624–5629, <https://doi.org/10.1039/c3nr04975b>.
- [29] H. Liu, D. Su, R. Zhou, B. Sun, G. Wang, S.Z. Qiao, Highly ordered mesoporous MoS₂ with expanded spacing of the (002) crystal plane for ultrafast lithium ion storage, *Adv. Energy Mater.* 2 (2012) 970, <https://doi.org/10.1002/aenm.2012.00087>.
- [30] A. Anto Jeffery, C. Nethravathi, M. Rajamathi, Two-dimensional nanosheets and layered hybrids of MoS₂ and WS₂ through exfoliation of ammoniated MS₂ (M = Mo, W), *J. Phys. Chem. C* 118 (2014) 1386–1396, <https://doi.org/10.1021/jp410918c>.
- [31] Y. Shu, W. Zhang, H. Cai, Y. Yang, X. Yu, Q. Gao, Expanding the interlayers of molybdenum disulfide toward the highly sensitive sensing of hydrogen peroxide, *Nanoscale* 11 (2019) 6644–6653, <https://doi.org/10.1039/c9nr00333a>.
- [32] N. Kumar, B.P.A. George, H. Abrahamse, V. Parashar, J.C. Ngila, Sustainable one-step synthesis of hierarchical microspheres of PEGylated MoS₂ nanosheets and MoO₃ nanorods: their cytotoxicity towards lung and breast cancer cells, *Appl. Surf. Sci.* 396 (2017) 8–18, <https://doi.org/10.1016/j.apsusc.2016.11.027>.
- [33] S. Anand, R.S. Sundararajan, C. Ramachandraraja, S. Ramalingam, R. Durga, Molecular vibrational investigation [FT-IR, FT-Raman, UV-Visible and NMR] on bis (thiourea) nickel chloride using HF and DFT calculations, *Spectrochim. Acta A* 138 (2015) 203–215, <https://doi.org/10.1016/j.saa.2014.11.032>.
- [34] J.E. Stewart, Infrared absorption spectra of urea, thiourea, and some thiourea-alkali halide complexes, *J. Chem. Phys.* 26 (1957) 248, <https://doi.org/10.1063/1.1743279>.
- [35] G. Aitken, J. Duncan, G. McQuillan, Normal co-ordinates for the planar vibrations of thiourea, and frequency assignment for selenourea, *J. Chem. Soc. A* (1971) 2695–2698, <https://doi.org/10.1039/j19710002695>.
- [36] Y. Zhang, P. Chen, F. Wen, B. Yuan, H. Wang, Fe₃O₄ nanospheres on MoS₂ nanoflake: electrocatalysis and detection of Cr(VI) and nitrite, *J. Electroanal. Chem.* 761 (2016) 14–20, <https://doi.org/10.1016/j.jelechem.2015.12.004>.
- [37] S.V.P. Vatikuti, C. Byon, C.V. Reddy, J. Shim, B. Venkatesh, Co-precipitation synthesis and characterization of faceted MoS₂ nanorods with controllable morphologies, *Appl. Phys. A* 119 (2015) 813–823, <https://doi.org/10.1007/s00339-015-9163-7>.
- [38] D.H. Youn, J.W. Jang, J.Y. Kim, J.S. Jang, S.H. Choi, J.S. Lee, Fabrication of graphene-based electrode in less than a minute through hybrid microwave annealing, *Sci. Rep.* 4 (2014) 5492, <https://doi.org/10.1038/srep05492>.
- [39] J. Ekspong, R. Sandström, L.P. Rajukumar, M. Terrones, T. Wågberg, E. Gracia-Espino, Stable sulfur-intercalated 1T' MoS₂ on graphitic nanoribbons as hydrogen evolution electrocatalyst, *Adv. Funct. Mater.* 28 (2018) 1802744, <https://doi.org/10.1002/adfm.201802744>.
- [40] X.-H. Zhang, N. Li, J. Wu, Y.-Z. Zheng, X. Tao, Defect-rich O-incorporated 1T-MoS₂ nanosheets for remarkably enhanced visible-light photocatalytic H₂ evolution over CdS: the impact of enriched defects, *Appl. Catal. B-Environ.* 229 (2018) 227–236, <https://doi.org/10.1016/j.apcatb.2018.02.025>.
- [41] X. Geng, Y. Jiao, Y. Han, A. Mukhopadhyay, L. Yang, H. Zhu, Freestanding metallic 1T MoS₂ with dual ion diffusion paths as high rate anode for sodium-ion batteries, *Adv. Funct. Mater.* 27 (2017) 1702998, <https://doi.org/10.1002/adfm.201702998>.
- [42] X. Chen, Z. Wang, Y. Wei, X. Zhang, Q. Zhang, L. Gu, L. Zhang, N. Yang, R. Yu, High phase-purity 1T-MoS₂ ultrathin nanosheets by a spatially confined template, *Angew. Chem. Int. Ed.* 58 (2019) 17621, <https://doi.org/10.1002/anie.201909879>.
- [43] H. Ren, Y. Pan, C.C. Sorrell, H. Du, Assessment of electrocatalytic activity through the lens of three surface area normalization techniques, *J. Mater. Chem. A* 8 (2020) 3154–3159, <https://doi.org/10.1039/c9ta13170a>.
- [44] X. Li, X. Lv, N. Li, J. Wu, Y.-Z. Zheng, X. Tao, One-step hydrothermal synthesis of high-percentage 1T-phase MoS₂ quantum dots for remarkably enhanced visible-light-driven photocatalytic H₂ evolution, *Appl. Catal. B-Environ.* 243 (2019) 76–85, <https://doi.org/10.1016/j.apcatb.2018.10.033>.
- [45] C. Feng, Z. Chen, J. Hou, J. Li, X. Li, L. Xu, M. Sun, R. Zeng, Effectively enhanced photocatalytic hydrogen production performance of one-pot synthesized MoS₂ clusters/CdS nanorod heterojunction material under visible light, *Chem. Eng. J.* 345 (2018) 404–413, <https://doi.org/10.1016/j.cej.2018.03.155>.
- [46] S. Zhang, H. Yang, H. Gao, R. Cao, J. Huang, X. Xu, One-pot synthesis of CdS irregular nanospheres hybridized with oxygen-incorporated defect-rich MoS₂ ultrathin nanosheets for efficient photocatalytic hydrogen evolution, *ACS Appl. Mater. Interfaces* 9 (2017) 23635–23646, <https://doi.org/10.1021/acsami.7b03673>.
- [47] Q. Yue, Y. Wan, Z. Sun, X. Wu, Y. Yuan, P. Du, MoP is a novel, noble-metal-free cocatalyst for enhanced photocatalytic hydrogen production from water under visible light, *J. Mater. Chem. A* 3 (2015) 16941–16947, <https://doi.org/10.1039/c5ta03949e>.
- [48] S. Liu, N. Zhang, Z.-R. Tang, Y.-J. Xu, Synthesis of one-dimensional CdS@TiO₂ core-shell nanocomposites photocatalyst for selective redox: the dual role of TiO₂ Shell, *ACS Appl. Mater. Interfaces* 4 (2012) 6378–6385, <https://doi.org/10.1021/am302074p>.
- [49] Z. Zhao, J. Wu, Y.-Z. Zheng, N. Li, X. Li, X. Tao, Ni₃C-decorated MAPbI₃ as visible-light photocatalyst for H₂ evolution from HI splitting, *ACS Catal.* 9 (2019) 8144–8152, <https://doi.org/10.1021/acscatal.9b01605>.
- [50] X. Wang, H. Wang, H. Zhang, W. Yu, X. Wang, Y. Zhao, X. Zong, C. Li, Dynamic interaction between methylammonium lead iodide and TiO₂ nanocrystals leads to enhanced photocatalytic H₂ evolution from HI splitting, *ACS Energy Lett.* 3 (2018) 1159–1164, <https://doi.org/10.1021/acsenenergylett.8b00488>.
- [51] S. Park, C. Kim, S. Park, N. Oh, U. Kim, J. Lee, J. Seo, Y. Yang, H. Lim, S. Kwak, G. Kim, H. Park, Phase engineering of transition metal dichalcogenides with unprecedentedly high phase purity, stability, and scalability via molten-metal-

- assisted intercalation, *Adv. Mater.* 32 (2020) 2001889, <https://doi.org/10.1002/adma.202001889>.
- [52] G. Ramasamy, S. Meenakshisundaram, Synthesis, growth, characterization and crystal structure of zinc cadmium thiourea complex $\text{Zn}_{0.625}\text{Cd}_{1.375}(\text{CS}(\text{NH}_2)_2)_9.4(\text{SO}_4)$, *J. Cryst. Growth* 377 (2013) 197–202, <https://doi.org/10.1016/j.jcrysgro.2013.05.021>.
- [53] H. Wang, W. He, X. dong, H. Wang, F. dong, In situ FT-IR investigation on the reaction mechanism of visible light photocatalytic NO oxidation with defective g- C_3N_4 , *Sci. Bull.* 63 (2018) 117–125, <https://doi.org/10.1016/j.scib.2017.12.013>.